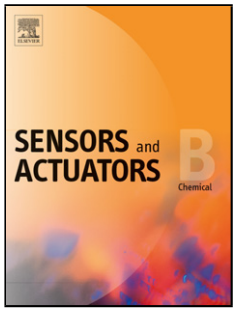

Title: Enhanced response and selectivity of H_2S sensing through controlled Ni doping into ZnO nanorods by using single metal organic precursors

Authors: Matin Roshanzamir Modaberi, Reza Rooydell, Sanjaya Brahma, Amos A. Akande, Bonex W. Mwakikunga, Chuan-Pu Liu

PII: S0925-4005(18)31222-X
DOI: https://doi.org/10.1016/j.snb.2018.06.117
Reference: SNB 24954

To appear in: *Sensors and Actuators B*

Received date: 6-1-2018
Revised date: 25-6-2018
Accepted date: 26-6-2018

Please cite this article as: Modaberi MR, Rooydell R, Brahma S, Akande AA, Mwakikunga BW, Liu C-Pu, Enhanced response and selectivity of H_2S sensing through controlled Ni doping into ZnO nanorods by using single metal organic precursors, *Sensors and Actuators: B. Chemical* (2018), https://doi.org/10.1016/j.snb.2018.06.117

Enhanced response and selectivity of H_2S sensing through controlled Ni doping into ZnO nanorods by using single metal organic precursors

Matin Roshanzamir Modaberi [a], Reza Rooydell [a], Sanjaya Brahma [a], Amos A. Akande [b], Bonex W. Mwakikunga [b], Chuan-Pu Liu [a,c]*

[a] Department of Materials Science and Engineering, National Cheng Kung University, Tainan, 70101, Tainan, Taiwan.

[b] DST-CSIR National Centre for Nanostructured Materials, Council of Scientific and Industrial Research, Pretoria 0001, South Africa.

[c] Hierarchical Green-Energy Materials (Hi-GEM) Research Center, National Cheng Kung University, Tainan, 70101, Tainan, Taiwan.

Corresponding author: cpliu@mail.ncku.edu.tw, Tel. No: +886-6-2757575-62943

Highlight

- Accurately controlling the amount of Ni doped into ZnO nanorods using single metal-organic hybrid.
- Study of the effect of Ni doping in ZnO nanorods on gas sensing.
- Determination of optimum Ni content in ZnO nanorods and optimum temperature in achieving the highest gas sensitivity.
- Analysis of the involved reaction rates of the adsorption and desorption of H_2S gas in the kinetic process.
- Proposal of the enhancement mechanism of H_2S gas sensing by Ni doped ZnO nanorods.

Abstract

We report on enhancing the selectivity and response of room (23 °C) and high temperature H_2S gas sensing through controlled Ni doping (0 to 10 at%) into ZnO nanorods (NRs) grown with a facile solution growth method using a single hybrid bimetallic metal-organic precursor (nickel/zinc acetylacetonate). The morphology, microstructure, surface chemistry and photoluminescence properties of the as-grown NRs are extensively examined. The gas sensing results are discussed in terms of doping concentration, operating temperature, gas type, gas concentrations and relative humidity. The optimal response toward 100 ppm of H_2S reaches 3.1 at 23 °C and increases to 45.3 at 200 °C for 8 at% Ni-doped ZnO NR sensors, where the corresponding response/recovery time at 23 °C and 200 °C also reaches 76/160 and 48/60 seconds, respectively. The same sensor exhibits high H_2S selectivity over other gases, including CH_4, CH_3OH and C_2H_5OH. The enhancement of gas sensing is attributed to increasing the number of active sites for adsorption of oxygen and target gases on the surface through incorporation of Ni^{3+} over Ni^{2+} ions. At 23 °C, the sensing mechanism is related to the formation of a 7 nm-thick ZnS layer over the NRs through reactions between H_2S and adsorbed oxygen.

Key words: ZnO nanorod ZnS layer Metal-organic precursor H_2S sensor

1. Introduction

Over recent years, detection and constant monitoring of hazardous air pollutants, toxic gases, and volatile organic gases have become of paramount importance in the societal effort to create a safe and healthy environment [1]. For this purpose, various types of gas sensors have been developed based on different signals originated from gas interactions with either sensing materials or probing sources. Among them, chemiresistive sensors present unique advantages due to their simple implementation and low manufacturing cost combined with good sensitivity, selectivity, and reliability for real-time monitoring, where semiconducting metal oxides (SMOs) represent the most popular materials to operate at high temperatures. However, the common chemisorption gas sensing mechanism often results in long response and recovery times [2,3].

Malodorous, toxic, and inflammable H_2S gas can be generated from the decomposition of organic compounds, from sewage and rubbish dumps, and from the biogas resulting of biowaste. Since the presence of H_2S gas can lead to catalyst deactivation, environmental pollution, and especially pipeline corrosion [4], highly sensitive and reliable H_2S sensors are in great demand for hazard prevention or control. Currently, H_2S gas can be monitored using chemiresistive sensors made of TiO_2 [5], WO_3 [6], ZnO [7] CuO/SnO_2 [8], α-Fe_2O_3 [9], and β-$AgVO_3$ [10]. Most H_2S gas sensors, have been determined to operate in the range of 150 - 450 $^{\circ}$C. However, still to take into consideration specific harsh conditions or safety concerns, the development of room temperature H_2S gas sensors is an urgent issue.

ZnO semiconductors have been regarded as ideal candidates for H_2S recognition due to advantages such as high temperature stability, facile fabrication, tunable conductivity by doping, and availability of a variety of surface treatments [11-12]. In the literature, the effect of high temperatures on the enhance gas sensing response has been nearly confirmed; however, limited studies have reported such effects at low temperatures [13-15]. To enhance gas sensitivity at room temperature, especially in the case of ZnO, doping might provide additional functions, including modifying the surface chemistry for chemisorption and boosting the conductivity of bulk ZnO. In addition, the additional optical, electrical, and catalytic properties of ZnO can be tailored by introducing relevant doping agents. Regarding doping technology, many methods have been reported, including sol-gel [16], co-precipitation [17], plasma-enhanced chemical vapor deposition [18], magnetron sputtering [19] thermal decomposition [20] and flame spray pyrolysis [21], etc. Nevertheless, all the aforementioned methods often provide limited control over the doping concentration due to the irrational interplay between two different metal precursors. Since the true amount of doping concentration bears no direct relationship with the relative concentration in the precursors during synthesis, there still remains the main challenge to gain control over accurate and systematic doping concentrations in ZnO nanomaterials.

Herein, we attempt to provide a systematic, comprehensive way to study the dependence of Ni doping in ZnO NRs on H_2S gas response with various Ni doping concentrations as well as relative humidity (RH) level. Hydrothermal synthesis at low temperature is employed by using well-characterized single bimetallic metal-organic precursors containing both Zn and Ni in various ratios, as described previously [22]. The proposed method allows the physical properties of doped ZnO NRs to be studied with Ni doping concentrations over a wide range in a controlled manner

specifically for gas sensing applications. The results demonstrate excellent reliability and high H_2S gas response at high temperatures and relatively acceptable responses at room temperature (23°C), an important characteristic for environmental protection and monitoring human health conditions. The results suggest that an appropriate amount of Ni dopants in ZnO NRs may effectively increase the number of surface active sites and charge transport for improving gas sensing performance and that this viable approach thus may shed light on developing a highly sensitive and selective room temperature (23 °C) H_2S gas sensors platform.

2. Experimental

2.1. Preparation of Ni-doped ZnO NRs

All the chemicals used in this study were of analytical grade purchased from Merck, Fluka without further purification. The growth scheme is described as follows: the solid metal organic precursors as diaquabis [zinc(II)-nickel(II)] acetylacetonate hybrid organic-inorganic complexes [$Ni_XZn_{1-X}(C_5H_7O_2)_2{\cdot}2H_2O$] ($N_XZ_{1-X}$ AA$\cdot 2H_2O$) (x=0-0.1) were synthesized through chemical method by mixing $Zn(NO_3)_2{\cdot}6H_2O$, (99.0%) and $Ni(NO_3)_2{\cdot}6H_2O$ (99.0%) in different ratios as the starting precursor materials. The detailed syntheses and characterizations of the above materials have been reported elsewhere [23].

In a typical procedure, 0.25 M of $N_XZn_{1-X}AA{\cdot}2H_2O$ was dissolved in distilled (DI) water/ethanol (H_2O-EtOH) solution under magnetic stirring for 15 minutes. silicon substrate ($1cm^2$) with a sputter-coated ZnO film was placed in 20 ml of solution inside a glass bottle, which was then tightly sealed. Subsequently, the bottle was slowly heated up to 80 °C and maintained at this temperature for 1 hour to grow the Ni-doped ZnO NRs. Finally, the products were washed with DI-water to remove any residual organics and dried at 120 °C in air for half an hour. Table 1 compares the Ni concentration in the NZAA precursors and the resulting NRs measured using energy dispersive X-ray spectroscopy (EDX) for a series of samples. The results reveal that the Ni doping concentration in the ZnO NRs derived by using single metal-organic precursors matched well with the Ni atomic percent in the NZAA precursors, demonstrating the great control of the doping concentration over a large percentage using this facile method.

The crystal structures of all the as-synthesized Ni doped ZnO NRs were analyzed by employing X-ray diffraction (XRD) with a Bucker AXE D8 GADDS micro diffractometer, using CuKα radiation (λ = 1.5418 Å) at 30 kV and 15 mA. The morphology and microstructure were characterized using scanning electron microscopy (SEM; HITACHI SU 8000) and transmission electron microscopy (TEM; JEOL 2100F), respectively, while EDX in the SEM and TEM was employed to study the sample composition. The surface chemical properties of the as-synthesized samples were studied in detail using X-ray photoelectron spectroscopy (XPS: VG ESCA-210D). The photoluminescence (PL) spectra were acquired using an He-Cd excitation source (325 nm) to examine the optical properties.

2.2. Sensor fabrication and gas sensing measurement

We used two different systems to sense inorganic gases and volatile organic liquid (VOL), where two laboratories have worked together, with their own facilities and a preliminary choice of each of the two systems. The testing data on inorganic gases were obtained through a gas sensing station at the Council of Scientific and Industrial Research *(*CSIR) laboratories in South Africa, while testing data on VOL were taken from the home-made equipment in our own lab. The precursor solution was taken in a glass bottle and the Si substrate sputtered-coated with ZnO seed layer was put upside down at 80 $^{\circ}$C as described in section 2.1. During the growth process, Ni doped ZnO NRs were grown on the substrate and the remnants (Ni doped ZnO powder) settled at the bottom of the glass was collected by evaporating all the solvents. The coatings obtained on the substrate were used for organic gas sensing in our laboratory and powder materials were used for inorganic gas sensing in CSIR, South Africa. The powder materials were dispersed in certain concentration of alcohol and then drop coated on the gas sensing electrode as described below.

2.2.1 Inorganic sensors

Fig. 1(a) shows the responses of inorganic gases of CH_4 and H_2S for various concentrations (5-100 ppm) at different temperatures of 23 $^{\circ}$C, 100 $^{\circ}$C, 200 $^{\circ}$C, 300 $^{\circ}$C and 350 $^{\circ}$C. Different concentration of Ni doped ZnO NRs powder varying from 0 to 10 at% prepared to deposit it on an alumina substrate. Finally, (NRs) powder was slightly dampened and disperse, in ethanol to making a thick paste of it on the Al_2O_3 substrates having interdigitated Pt electrodes on its top

surface. As a way to enhance uniformity of samples in terms of the amount of tubes on each device as well as avoid too much resistance fluctuations between different samples a fixed concentration of 0.01 mg/mL of the Ni doped ZnO in ethanol was maintained throughout and only two droplets were put on each device using a micro pipette. The inorganic gas sensing measurements were carried out using a KSGAS6S gas sensing station (KENOSISTEC, Italy). The resistance of the sample was collected in the temperature range of 298 to 623 K as a function of temperature. The sensors were heated to 130 $^{\circ}$C for 30 min by heating in an oven and solution was evaporated from the deposited films.

It is admittedly very difficult to distinguish between the heating element temperature and the actual surface temperature of the sensing nanorods. We did do not have a surface temperature sensor for us to track the nanorods temperature in-situ. This was pre-calibrated by the manufacturer. However, we have performed temperature calculation ex-situ by employing an infrared laser pyrometer at a corresponding heater current on a corresponding Al_2O_3 (alumina)-based strip sensor which is in many ways similar to this commercial sensor electrode used here; from these experiments we obtain the calibration curve for the nanoparticle surface temperature.
The gas sensing response of the device was followed by recording the variation in the resistance of the sensors monitored using a keithley 6487 picoammeter/voltage source metre attached with the sensing station. The sensing element was first stabilized in dry synthetic air (80% N_2 and 20% O_2) at 500 sccm (standard cubic centimeters per minute) for about 2h and fixed to obtain a baseline resistance. After attaining the stable baseline resistance, the sensing element was exposed to various concentrations of the gas mixture (synthetic air and H_2S gas) delivered from one side of the sensor device. The gas sources are commercially available in gas cylinders. The transient resistance of the samples was measured and recorded in dry air at the gas flow rate of 250 mL/min.

Briefly, the sensor was mounted in a double-walled stainless-steel chamber, which includes the basic measuring circuit for metal-oxide gas sensors. Fig. 1(b) displays the basic measuring electronic circuit of the gas sensor, where, R_L is a load resistor connected in series with the gas sensor, R_L =(V-Vs)/I. R_L is about 5 MΩ. The response of the sensor was measured by monitoring the voltage changes of R_L. V_{RL} is the voltage on R_L. V_C is the constant voltage (V_C =5V) applied on the R_L and the sensor. The signal voltage $V_S = V_C - IR_L$, and Rs = Vs/I is the resistance of the sensor, Rs = Ra (in air) and Rs = Rg (in target gas). Through varying the heating voltage (V_H), different operating temperatures were obtained.

2.2.2 VOL organic sensors

On the other hand, Fig. 1(c) shows the VOL sensor device devised to obtain the response of organic gases of CH_3OH and C_2H_5OH with the same testing conditions in temperate and gas concentration as applied for inorganic gases. Two Ti/Au electrodes were patterned using interdigitated electrodes on top of an Ni-doped ZnO NRs thin film, grown on silicon coated with sputtered ZnO that was 2×2 cm and 300 nm thick. Both Ti/Au electrodes were deposited using the Precision Etching Coating System (PECS) under a working voltage of 5kV, where the thickness of the Ti/Au electrodes were 10nm/100nm, respectively, followed by mounting conductive wires with silver paste. The set was then placed inside of a closed chamber.

The VOLs response and recovery were measured in static mode (air inlet and outlet closed) and dynamic mode (air inlet and outlet open), respectively. A Keithley 2400 source meter was used to record the induced resistance change with time, which was controlled by a computer with resistance screening software. During the response in static mode, different concentrations of the target liquid were dropped into the closed chamber via a micro-injector through a rubber plug and allowed to evaporate on the hot flat heater at 50 $^{\circ}$C. The vaporized VOL was allowed to interact with NRs devices for 10 min before purging the chamber with air. During the recovery in dynamic mode, the vaporized VOL was evacuated using a rotary pump through air outlet and fresh air was allowed to flow in through the air inlet simultaneously for 10 min. The target gases were then detected by the Ni-doped ZnO sensing devices through displaying the resistance with time to monitor the response of the devices upon exposure to the gas. All the measurements were performed under 1atm pressure at room temperature (23 $^{\circ}$C). The gas-sensing response (S) for reducing gas is defined as

$$S = Ra/Rg, \qquad (1)$$

where Ra and Rg represent the resistance of the sensor in dry air and the target gas, respectively.

3. Results and discussion

3.1. Structural and morphological characterization

Fig. 2 illustrates the microstructure analysis of all the as-grown NRs obtained by combining SEM, EDX and XRD. Fig. 2(a-c) show the SEM images of the as-grown un-doped and Ni-doped ZnO NRs with Ni concentrations of 8% and 10%, respectively. It can be seen that the NRs tend to grow shorter and coarser with increases in the Ni content. The average NR length is estimated to decrease from approximately 800 nm for the un-doped NRs (Fig. 2(a)) to around 700 and 600 nm with Ni doping levels of 8% and 10%, respectively (Fig. 2(b-c)), while the average diameter increases from 100 nm for the undoped ZnO NRs to 250 nm for the 10% Ni-doped ZnO NRs. The main growth from the hydrolysis reaction of the bimetallic precursors, releasing both Zn^{2+} and Ni^{2+} ions in the solution, leads to the formation of various metal hydroxides for the nucleation and growth of the oxide NRs. The concentration and distribution of the anions including $CH_3CO\overline{O}$ and $O\overline{H}$ in the solution can affect the morphology, size, and density of the NRs. Fig. 2(d) shows the typical EDX spectra of the un-doped and Ni- doped ZnO NRs with various amounts of Ni ranging from 1 to 10%. The EDX analysis indicates that the obtained NRs are composed of Zn, Ni, and O in addition to Si derived from the substrate, where the intensity ratio of Ni to Zn exhibits an increasing trend with increases in the Ni dopants, as shown in the inset. The Ni doping concentration is then calculated to be close but slightly smaller than the nominal value as compared in Table 1. The X-ray diffraction spectra in Fig. 2(e) of the un-doped and Ni doped ZnO NRs from 1 to 10% confirm that all the ZnO NRs are in the form of a hexagonal wurtzite structure (JCPDS Card No: 00-001-1136). It is worth noting that no secondary phases such as NiO are detected up to 8% suggesting that all the Ni ions successfully occupy the ZnO lattice sites. However, NiO clusters start to form at 10% Ni doping, evidenced by two new peaks at 38.7˚ and 43.3˚ corresponding to (111) and (200) planes of cubic NiO phase (JCPDS 78-0643), respectively. This suggests that 10 % Ni doping is beyond the solubility limit of Ni in the ZnO host matrix. Moreover, because of the smaller radius of Ni^{2+} (0.69 Å) as compared to that of Zn^{2+} (0.74 Å), the replacement of Zn^{2+} by Ni^{2+} should lead to a slight decrease in the lattice parameters, causing a shift of the diffraction peaks toward larger angles. Fig. 2(f) shows an enlarged view of the first three diffraction peaks in an angle range of 30˚-38˚ for the Ni-doped ZnO NRs with different Ni concentrations (0-10%), testifying to the successful Ni-doping inside the ZnO NRs from the peak shift. For example, the ZnO $(10\bar{1}1)$ diffraction peak shifts from 36.05˚ for the un-doped ZnO to 36.21˚ and further to 36.28˚ in the case of the 3% and 8% Ni-doped ZnO NRs, respectively. Nevertheless, the peak shift backward for even higher Ni doping concentrations of 10% correlates

to the onset of the formation of the second phase of NiO clusters [24, 25]. Therefore, when the Ni content provided is more than can be dissolved in the ZnO lattices, thus NiO will precipitate depleting the fraction of Ni ions substituting for ZnO lattice sites.

The TEM bright-field image in Fig. 3(a) shows the typical morphologies of NR aggregates from the as-synthesized 5% Ni-doped ZnO NRs. The products are composed of small, tightly-packed, polydispersed NRs. Fig. 3(b) shows a high-magnification TEM image of a typical single NR, with a diameter of ~125 nm and a length of ~750 nm. The corresponding selected-area diffraction pattern in the right inset of Fig. 3(b) testifies to the existence of only the wurtzite phase. The high-resolution TEM image of selective NR in the left inset of Fig. 3(b) indicates that the NR is a single-crystalline structure, growing along a [0001] direction in which the lattice spacing of 2.46 Å and 2.80 Å can be assigned to the (0002) and $(10\bar{1}0)$ planes, respectively.

Fig. 4(a) shows the overlay XPS survey spectra of un-doped and Ni-doped ZnO NRs of various concentrations where only Zn 2p, Ni 2p, and O1s peaks are detected. Fig. 4(b) further examines the Zn 2p peaks of all the samples. In comparison with the un-doped ZnO NRs, where the Zn $2p_{3/2}$ and Zn $2p_{1/2}$ core levels are centered at around 1021.6 eV and 1044.7 eV, respectively, these values are all shifted to higher bonding energies by ~0.2 eV for 3%, ~0.4 eV for 5%, and ~0.6 eV for 8% Ni-doped ZnO, but the peak difference between the two core levels as a spin-orbital splitting energy of 23.1 eV is maintained. The change in the binding energy of the Zn $2p_{3/2}$ could be attributed to the effects of Ni doping. The XPS spectra of the O1s core levels are compared in Fig. 4(c), where each spectrum can be deconvoluted into two sub-peaks, as numerated in Fig. 4(d) for 5% Ni-doped ZnO NRs using Gaussian curve fittings. The sub-peaks in Fig. 4(d) centered at ~530.1 eV and 531.5 eV can be assigned to O atoms at regular lattice sites (O_L) [25] and oxygen-deficient sites (O_V) [26], respectively. Apparently, these two peaks of the un-doped ZnO centered at 530.5 eV and 531.7 eV shift toward lower binding energies with Ni doping. In addition, the peak area on the high binding energy side increases dramatically with increases in Ni concentration as the intensity ratio of O_V/(Zn+Ni) increases from 0.5 to 2.4 from 3% to 8% Ni doping (see insets), indicating an increase in oxygen vacancies accompanied by the incorporation of Ni. This is consistent with the PL analysis (discussed below), where an O_V-related green emission is dominant. The Ni2p spectra of the 3%, 5% and 8% Ni-doped ZnO NRs are further examined in Fig. 4(e), including Ni $2p_{3/2}$ and Ni $2p_{1/2}$ core levels and a shakeup satellite peak. From the spectra,

Ni ions are proven to have successfully substituted for Zn sites based on the spin-orbital splitting energy of 17.8 eV distinct from the metallic Ni of 17.27 eV and the presence of the shakeup satellite peak at 861.37 eV, ascribed to charge-transfer transition in the final state involved with the hybridization of O (2p) and Ni (3d) [27]. In addition, $Ni2p_{3/2}$ peaks can be further decomposed into two sub-peaks at 855.6 eV and 857.3 eV, corresponding to the Ni^{2+} and Ni^{3+} valence state, respectively, as shown in (Fig. 4(f-h)) for the 3%, 5% and 8% Ni-doped ZnO NRs, respectively. The Ni ions exist predominantly as the divalent states for the ZnO NRs with lower Ni concentrations; however, the fraction of the trivalent state increases with increases in the Ni content. The relative area ratio of Ni^{3+}/Ni^{2+} for 3%, 5% and 8% Ni-doped ZnO NRs is 3.5, 5.7, and 8, respectively.

The Ni doping induced defects that could play important roles in enhancing gas sensing properties is studied through room temperature (23 $^{\circ}$C) PL spectroscopy, as shown in Fig. 5(a) for the un-doped and various Ni-doped ZnO NRs. The UV emission peaks at ~375 nm result from near-band edge emissions or free exciton emissions [28]. A red shift in the UV emission peak is observed up to 8%, indicative of a decrease in the band gap. The red shift in the band gap is presumably attributed to the sp-d exchange interactions between the band electrons and the localized d electrons of the Ni^{2+} ions substituting for Zn ions, implying the successful incorporation of Ni ions into the Zn lattices of the ZnO matrix [29]. The visible luminescence reveals a strong green emission, which gradually shifts toward a yellow emission and then an orange-red emission with increasing Ni doping concentrations up to 8% [30].

Moreover, the strong visible emissions are further Gaussian deconvoluted to examine the defect-related luminescence shown in Figs. 5 (b-d) for the un-doped, 8% and 10% Ni doped ZnO NRs, respectively. For example, in Fig. 5(b), possible emissions in a broad visible range of the un-doped ZnO NRs can be decomposed into three sub-peaks at ~450 nm, ~544 nm, and 585 nm, where the first peak is a blue emission, originating from the presence of Zn_i-related surface defects [26]. The second broad peak is called a green emission band or a deep-level emission caused by oxygen vacancies (V_O^x, $V_O^{\cdot\cdot}$) and zinc vacancies ($V_{Zn}^{\prime/\prime\prime}$), followed by the yellow emission (above 580 nm) ascribed to oxygen interstitials ($O_i^{\prime/\prime\prime}$). [31]. It is noted that the ratio of defect to UV emission intensity increases from 1.1 for the un-doped ZnO NRs to 1.8 for the 8% Ni doped NRs while the ratio decreases to 1.6 for the 10% Ni content due to a reduced doping effect. The increase in the

green emission intensity with Ni content accompanied by the dramatically increased ratio of Ni^{3+} to Ni^{2+} in the XPS results confirm the increase of defects with increases in the Ni doping concentration. It has been reported that vacancy and interstitial-related defects in ZnO can remain stable at room temperature (23°C) as measured by electron paramagnetic resonance [32].

3.2. Room temperature gas sensing

At 23 °C, changes of transient resistance of the ZnO NRs sensors with different Ni-doped ZnO NRs at 5-100 ppm H_2S, for comparison are shown in Fig. 6(a). Seven pulses for each sensor exhibit a decrease in resistance with increasing H_2S gas concentrations. Most intriguingly, the gas response increases with Ni doping concentrations up to 8% for each gas concentration and then decreases at 10% Ni, clearly demonstrating the enhancement of gas response by Ni doping and a close correlation between effective Ni doping concentrations and gas response, which is subsequently deteriorated by the formation of the second phase as Ni of more than 8% is incorporated. Fig. 6 (b) shows the corresponding dynamic response of Fig. 6(a). The maximum response appears to be 3.1 when 8% Ni is doped in ZnO at 100 ppm H_2S gas. Fig. 6(c) shows resistance of the Ni-doped NRs sensor with various Ni concentrations in response to 100 ppm of different gas species. The inset compares the response of various Ni-doped ZnO sensors to 100 ppm of different gases at 23 °C, including H_2S, CH_4, CH_3OH, and C_2H_5OH. The results are strikingly consistent in that response increases monotonically with Ni content up to 8% to all the target gases, strongly suggestive of similar working mechanism of sensor response to different types of gases as a result of the Ni doping effect. Ultimately, through systematic study of Ni doping effects on ZnO sensors, we concluded that these sensors can be used for the measurement concentrations values of mentioned reducing gases up to 100 ppm, with a better sensitivity with H_2S.

3.3. High temperature gas sensing

All the sensors tested at an elevated temperature of 200 °C in Fig. 6(d) shows the same trend of response dependence to Ni content and gas concentration as mentioned at room temperature (23 °C) in Fig. 6(a). Fig. 6(d) shows the transient resistance of the un-doped ZnO and various Ni-doped ZnO NRs to different H_2S gas concentrations ranging from 5 ppm to 100 ppm at 200 °C. The corresponding response curves as a function of H_2S concentration are depicted

in Fig. 6(e) which is indicates the highest response occurs for 8% Ni doping ZnO. The response of the 8% Ni-doped ZnO NRs is the most enhanced in a nonlinear manner compared to other sensors with less doping concentrations. One interesting feature that should be noticed is the distinct response behavior. As shown in Fig. 6(e) inset, for smaller gas concentrations or less Ni content, the response gradually increases before saturation, resembling those taken at room temperature (23 °C), but raises sharply (as indicated by A) followed by a gradual decrease (as indicated by B) for larger gas concentrations or more Ni content. Presumably, while a single mechanism or gas is involved in the low concentration cases, there seems to be two mechanisms or gases in competition in the high concentration cases, which include the oxygen from the oxidizing gas and the H_2S from the reducing gas. Due to the lower adsorption energy of H_2S, H_2S might come to thermal equilibrium in a shorter time than oxygen, but the true reaction rate depends on the concentration of H_2S in the gas and the available surface sites that could trap it. In the case of a high H_2S concentration or high trapping cites on the surface as occur with high Ni doping concentrations, the reaction rate of H_2S at the surface becomes much higher than the O_2 adsorption, leading to kink behavior caused by distinct two-step reactions, which is manifested with the features present during high temperature sensing. We have also performed the cycle test to testify the durability of our sensor devices as shown in Fig. 6(f) demonstrating the response curves of the 8% Ni doped ZnO sensor for two cycles to each of H_2S gas concentration at 23 °C, while the inset shows the same for three cycles to 100 ppm H_2S gas at 200 ºC. The sensor has almost the same response between the two and three cycles, and the response curve recovers back to the baseline in air when the test gas is released. These clearly proves the stability of the sensor and reproducibility of the obtained results at mentioned temperatures.

3.4. Influence factors on gas sensing

During measurements, the RH levels were monitored constantly by a standard hygrometer (KENOSISTEC, Italy) at 21 ºC. In order to avoid the influence of humidity variation on the sensor response, H_2S gas was introduced only until the sensor resistance became stable at desired RH. Under humid environment, displacement of chemisorbed oxygen species by multi-layered physiosorbed water molecules have been known as the humidity detection mechanism [33]. Obviously, the effect of the ambient humidity on the response at room temperature is much more significantly than that at higher temperatures. The inset of Fig. 6(b) shows the response to 100

ppm H_2S along with other gases for 8% Ni-doped ZnO NRs as a function of RH values between (25-80 %) at 23 ºC. The results of response to gases shows increase to the maxima with rise of the RH value up to ~52% and exhibit decreasing trend with increasing relative humidity. In fact, H_2O molecules are in competition with oxygen for occupying the surface sites. With increasing humidity, more H_2O molecules adsorb so that density of the adsorbed oxygen is reduced leading to decrease in the sensor response. However, our results suggest that the adsorption and desorption mechanism involving water molecule with reducing gas is more complex and require more further studies.

Fig. 7(a) shows the response of various Ni-doped ZnO sensors to 100 ppm H_2S as a function of operation temperature, where the response increases with Ni concentration up to 8% and with temperature up to an optimum operating temperature of 200 °C. Fig. 7(b) shows the response of the 8% Ni-doped ZnO sensor to H_2S gas concentration for various operating temperatures. As expected, the response has a positive relationship with gas concentration for all temperatures under consideration. As seen in Fig. 7(a) and (b), the maximum response of all the sensors is found at 200 °C, indicating the fastest surface chemical reactions with good charge carrier mobility at this optimum temperature. As the temperature becomes higher than 200 °C, oxygen adsorption may be quicker than oxygen desorption, so less adsorbed oxygen molecules are available to react with the target gas, causing decreasing response at higher temperatures [34].

The response time in the case of adsorption ($t_{90\%}$) and the recovery time in the case of desorption ($t_{10\%}$) are dependent on gas species, gas concentration, doping concentration and operation temperature. Fig. 8(a) shows the typical response and recovery time vs. operation temperatures at 23 °C, 100 °C, 200 °C, 300 °C, and 350 °C for the 8% Ni-doped ZnO sensor at 100 ppm of H_2S. The results of all the concentrations of H_2S show higher temperature results in the faster response and recovery time so that the response time decreases from 76 s at 23 °C to 48 s at 200 °C and 36 s at 350 °C, while the recovery time decreases from 160 s at 23 °C to 60 s at 200 °C. The fast response and recovery process at higher temperatures could be attributed to fast surface chemical reactions, higher charge carrier mobility, and enhanced gas-phase diffusion. Fig. 8(b) shows the response and recovery time vs. H_2S gas concentration (5-100 ppm) for the 8% Ni- doped ZnO sensor at 23 °C and 200 °C, respectively. Both curves reveal faster response and recovery time

at 200 °C than 23 ºC, as expected. This phenomenon can be explained as follows: (1) adsorption and desorption processes are thermally activated and sensitive to the temperature. (2) The increased working temperature will accelerate the electron transition between the conductor band and the surface Fermi level, which could facilitate the desorption reaction [35]. Fig. 8(c) shows the response and recovery time vs. Ni content toward 100 ppm H_2S at 23 °C and 200 °C, respectively. The effect of Ni doping on response and recovery time for both temperatures shows the same trend, where the response and recovery time decreases with increases in Ni doping. Fig. 8(d) correlates the dependence of the sensor response time to 100 ppm H_2S at 23 °C on Ni content with an Ni^{3+}/Ni^{2+} ratio, indicating the reaction kinetics is directly related to the Ni^{3+}/Ni^{2+} ratio in accordance with more active sites created by Ni^{3+} ions through Ni doping. The higher Ni^{3+}/Ni^{2+} leads to a shorter response time, indicating the incorporation of Ni^{3+} could lead to a reduction in the activation energy of the surface chemisorption of the gases.

The activation energy of H_2S gas adsorption and desorption determines the reaction rate through the Arrhenius equation to be $R=R_o\ exp\ (-E/kT)$, where R is the reaction rate; R_o is chemical pre-exponential constant; K is the Boltzmann constant; T is absolute temperature, and E is the activation energy. Fig. 9(a) demonstrates the evaluation of activation energy from the linear fitting slope to the curve of Ln (R) vs 1/T in a temperature range of 23-350 °C for the 8% Ni-doped ZnO NRs under 100 ppm H_2S. Correspondingly, the adsorption and desorption energy is estimated to be 2.05 kJ/mol (correlation coeffication of 98%) and 4.80 kJ/mol (correlation coeffication 97%), respectively. This suggests that the involved reaction is chemisorption because it requires more energy to release adsorbed gases than gas adsorption.

With the same procedure, we evaluate the energy barrier of adsorbtion and desorbtion toward H_2S for the Ni-doped ZnO NRs with 3, 5, 8, and 10% Ni content as shown Fig. 9(b). When increasing Ni content from un-doped ZnO to 8% Ni-doped, the adsorption activation energy decreases up to 1.6 kJ/mol, while the desorption activation energy reduced up to 1.5 kJ/mol. The minimum activation energy occurs at 8% Ni content since 10% Ni content adversely boosts the activation energy. Consistent with the previous results, both the adsorption and desorption energies decrease progressively with Ni content, supporting the effective facilitation of H_2S gas sensing by Ni doping to ZnO NRs.

To understand more about H_2S sensing performance, our results are compared with recently reported data in Table 2. It can be clearly seen that not only the response of the Ni-doped ZnO sensors at 23 °C and 200 °C is obviously advantageous over the others, but also the corresponding response-recovery time is among the fastest, enabling Ni-doped ZnO NRs to have great potential to be applied in H_2S gas sensors.

3.5. Gas sensing mechanism

The adsorption can gradually change from physi-sorption to chemi-sorption with increasing operation temperatures to provide higher level of energy, accompanied by different degrees of charge transfer. In the regime of chemi-sorption at relatively high temperatures, a reducing gas, such as H_2S, in the presence of O_2 can be shown on the surface as follow:

$$O_{2\,(g)} + 2e^- \leftrightarrow O^-_{(ads)} \quad (2)$$

$$H_2S_{(g)} + 3O^-_{(ads)} \rightarrow H_2O_{(g)} + SO_{2(g)} + 3e^- \quad (3)$$

In the absence of a target gas, electrons are removed from Ni-doped ZnO NRs by the reduction of O_2 (reaction 2) resulting in the formation of O^- adsorbed species, and consequently, the conductance decreases. The temperature-dependent stable types of oxygen ions are O_2^- below 100 °C, O^- between 100 and 300 °C, and O^{2-} above 300 °C [43]. Therefore, at the optimum operation temperature of 200 °C, introduced H_2S gas should react with $O^-_{(ad)}$ (reaction 3), and electrons can be released into the depletion layer, leading to an increase in the conductance. Therefore, the response increases with increases in the concentration of H_2S gas or $O^-_{(ads)}$.

As for sensing to H_2S at room temperature, since reaction (3) cannot proceed at room temperature (23 °C), partial sulfuration of the sensing films could occur based on thermodynamic analysis. It has been reported that the change in the Gibbs free energy (ΔrG°) for the sulfuration reaction of Eq. (4) is -74.08 kJ/mol at 23 °C [44] indicating an exothermic and spontaneous reaction is favored at low temperatures [45]. However, the reactions between ZnO and other test gases are endothermic and cannot be spontaneous [13]. When exposing to H_2S and subsequent removal of it at room temperature, the following reactions would take place on the surface of the ZnO film.

$$ZnO_{(s)} + H_2S_{(g)} \rightarrow ZnS_{(s)} + H_2O_{(g)} \quad (4)$$

$$ZnS_{(s)} + 3/2O_{2(g)} \rightarrow ZnO_{(s)} + SO_{2(g)} \quad (5)$$

As a result, response to H_2S could be attributed to formation of the ZnS and this spontaneous reaction affords us an opportunity to obtain a thin ZnS layer at the interface between the ZnO nanorods and the H_2S gas. The formation process of the ZnS layer on the ZnO NRs is investigated using TEM in Fig. 10. According to reaction (4), the ambient humidity should decrease the response, or lower humidity should correspond to the higher response. However, the opposite is observed in this study (see Fig. 6(b) inset). Hence, here, we investigated the effect of humidity on the response of ZnO NRs sensors to H_2S through H_2S hydrolyzation-induced at 23 $^{\circ}$C.

3.5.1 H_2S hydrolyzation-induced enhanced gas sensing; role of ambient atmosphere

This study has demonstrated that the ambient humidity plays an important role in the sensing of Ni doped ZnO NRs to H_2S, especially at room temperature. Enhanced sensing of the ZnO thin film to H_2S at 23 $^{\circ}$C could be attributed to the humidity-induced H_2S hydrolyzation. Such hydrolyzation could lead to desorption of the oxygen chemisorbed on the ZnO and formation of water thin film on the ZnO surface, which significantly increase the response of the sensor. When H_2S reducing gas was injected into the test chamber with a certain relative humidity, the hydrolyzation or the reaction.

$$H_2S + H_2O_{(g)} \Leftrightarrow HS^- + OH^- + 2H^+ \quad (6)$$

would take place. The reaction of H_2S with H_2O molecules would produce HS^-, $OH^-$and H^+, (see Fig. S(a) in the Supporting Information, SI). The produced $HS^-$and H^+ would contact and react with the chemisorbed oxygen O_2^{x-} on the ZnO surface, including the following reactions:

$$HS^- + ZnO + H^+ \rightarrow ZnS\ (lattice) + H_2O_{(g)} \quad (7)$$

$$HS^- + 2O_2^{x-} + 3H^+ + ZnO \rightarrow ZnSO_4 + H_2O_{(g)} + H_{2(g)} + 2xe^- \quad (8)$$

Hydrolyzed HS^-could react with the ZnO and induce substitution of the divalent sulfur for oxygen in ZnO lattice or formation of the molecules ZnS in the ZnO lattice, which would also increase the conductance. In addition to, reaction (8) would form $ZnSO_4$ molecule on the ZnO film, and lead to release of the captured electrons back to the bulk and hence reduction of the resistance

of the ZnO film, (see the inset of Fig. S(b) in the Supporting Information). On the other hand, the hydrolyzed OH^-would adsorb on the ZnO surface, which would promote adsorption of H_2O molecules in the ambience or even formation of water thin film on the ZnO, especially under high relative humidity, (Fig. S(b)). This would decrease the resistance of the ZnO film. Subsequent removal of the gas H_2S, in addition to (5), the following reactions could occur.

$$ZnSO_4 + O_{2(g)} + 2OH^- + xe^- \rightarrow ZnO + O_2{}^{x-}{}_{(ad)} + SO_{2(g)} + O_{2(g)} + H_2O \quad (9)$$

It means that the oxygen in air would be chemisorbed back on the ZnO film, leading to increase of the film resistance. According to the above H_2S hydrolyzation-induced gas sensing mechanism, we can explain the responses of the ZnO to H_2S at room temperature in this study. In the environment with a certain of humidity, when the ZnO NRs sensor was exposed to the H_2S, reactions (6)-(8) would take place, which leads to the significant reduction of the resistance of the sensing film and hence high response, due to the desorption of the chemisorbed oxygen and formation of surface adsorbed H_2O (even water thin film). As for the ultra-high response, it should be attributed to the too thin skeleton of the mico/nanostructured ZnO film [33]. Evidence on the formation of S^{2-} and S^{6+} species has been shown by the XPS spectra recorded from the active layer after H_2S measurement (Figures S.(c) and S.(d)). Chemisorption occurs at relatively low % RH value to form two surface hydroxyls per water molecule as illustrated in Fig. S(e). In the chemisorbed layer, charge transport occurs by the hopping mechanism [46,47]. With increasing humidity levels, physisorption of water molecules takes place resulting in capillary condensation and conduction occurs mainly by the Grotthuss transport mechanism [48]. If the humidity is too high (higher than 52% RH in this study), however, it would not favor reactions (7)-(8) and induce gradual decrease of the response. Only a moderate humidity can lead to the highest response, as demonstrated in Fig. 6(b).

(Fig 10 (a-d)) shows the RT-TEM images of the 8% Ni-doped ZnO sensor before and after exposure to 100 ppm H_2S at 23 $^{\circ}$C for 3 h, demonstrating the formation of a thin ZnS layer. Fig. 10(a) shows some undulations on the rough surface (red arrows) before exposure to H_2S; nonetheless, the rod exhibits high crystallinity of the ZnO wurtzite structure shown in the corresponding HR-TEM image in Fig. 10(b). After exposure to H_2S 23 $^{\circ}$C, a continuous ~7nm thin film is formed at the surface of the NR, as shown in Fig. 10(c). The corresponding HR-TEM image shown in Fig. 10(c) is presented in Fig. 10(d), verifying the presence of the ZnS phase by

presenting lattice constants, where the marked interplanar *d* spacings of ~1.91 Å and ~1.76 Å correspond to the $(11\bar{2}0)$ and $(10\bar{1}3)$ lattice planes of WZ ZnS, respectively. The EDX spectra taken from the surface of the sensor before and after exposure to H_2S in Fig. 10(b) and d, respectively, clearly display sulfur only present after exposure, supporting the H_2S sensing mechanism at 23 °C.

4. Conclusion

We successfully synthesized ZnO NRs with systematic variations in Ni doping concentrations from 0 to 10 at% through the use of a solution method using bimetallic metal acetylacetonate precursor as a single source instead of using two different compounds. This complex is commonly called as bis (acetylacetonato- $\kappa^2 O,O'$) [zinc (II)/Nickel (II)], where both Zn and Ni atoms were applied at the center of the complex. Besides selective control over the atomic ratio of Ni to Zn in the bimetal, the fact that it is inexpensive, chemically safe, has an easy work-up process, high product yield, and short reaction time can be considered as advantages of the proposed method. XRD, XPS and PL measurements confirm the substitution of Zn by Ni in the hexagonal lattices. The sensing results demonstrate that an Ni-doped ZnO NR sensor under optimum doping of 8% Ni has the potential to sense H_2S gas with much higher response and a faster response as compared with un-doped ZnO NRs. The sensing mechanism to H_2S is introduced and the relative humidity level ~52% at 21 °C (determined by an in-built humidity sensor in the sensing chamber) represents the optimum response of the sensors. In this study the results show high sensibility of the sensors at 200 °C and the increase of oxygen vacancies and other defects introduced by Ni doping through Ni^{3+} ions will offer more active sites for the reactions so that the gas sensing properties of ZnO NRs will in turn be improved.

Acknowledgments

This work was financially supported by the Hierarchical Green-Energy Materials (Hi-GEM) Research Center, from The Featured Areas Research Center Program within the framework of the Higher Education Sprout Project by the Ministry of Education (MOE) in Taiwan. Also, the authors acknowledge the funding from the Ministry of Science and Technology (MOST), Taiwan, under grant MOST 104-2221-E-006-079-MY3.

Table 1 Comparison of expected and measured EDX results shown in Fig. 2(d) concentration of various Ni doped ZnO NRs.

Sample name, nominal Ni doping (%) in ZnO NRs	1% Ni	3% Ni	5% Ni	8% Ni	10 % Ni
Atomic percent of NAA in NZAA	1.5	3.50	5.50	8.50	10.50

Ni concentrations in ZnO NRs measured using EDX (at%)	1.01	3.10	5.10	8.02	10.21

Table 2 Comparison of reported H_2S sensing performance based on various ZnO nanostructures and ours. (a) The response time is defined as the time required to reach 90% of the full response

change in the sensor after the testing gas enters, and the recovery time is defined as the time taken to fall to 10% of its maximum response after the testing gas exits.

Sensing element	Fabrication method	Operating temperature (ºC)	Response/Gas conc.(ppm)	Response def. (S=)	Res./Rec.[(a)] time(s)	Ref.no
PPy/WO_3	UV polymerization	RT	5.3 /1	V_g/V_a	260/12600	[36]
quasi-2D CuO/SnO_2	Electrochemical deposition	RT	1.8/50	(ΔR/R)	180/500	[37]
Ni-doped ZnO NRs	Hydrothermal	23	3.1/ 100	(Ra)/Rg	76/160	This study
La-doped In_2O_3 (5.0 wt.%)	Hydrothermal	125	0.86/50	(ΔR/Ra)	5/ 4 min	[38]
Polypyrrole (20%)/WO_3	Chemical oxidation polymerization and Emulsion	90	8.600/1000	Vg/Va	88/60	[39]
α Fe_2O_3 nanoparticles	post-thermal annealing	300	~5.3/10	Ra/Rg	30/5	[40]
CuO NP decorated porous ZnO NRs	Hydrothermal	100	40/ 100	Ra/Rg	120/70%	[41]
ZnO nanorod-bundle	Hydrothermal	350	~3/50	(Ig_Ia)/Ia	~220/~950	[42]
Ni-doped ZnO nanorod	Hydrothermal	200	45.3/100	(Ra)/Rg	48/60	This study

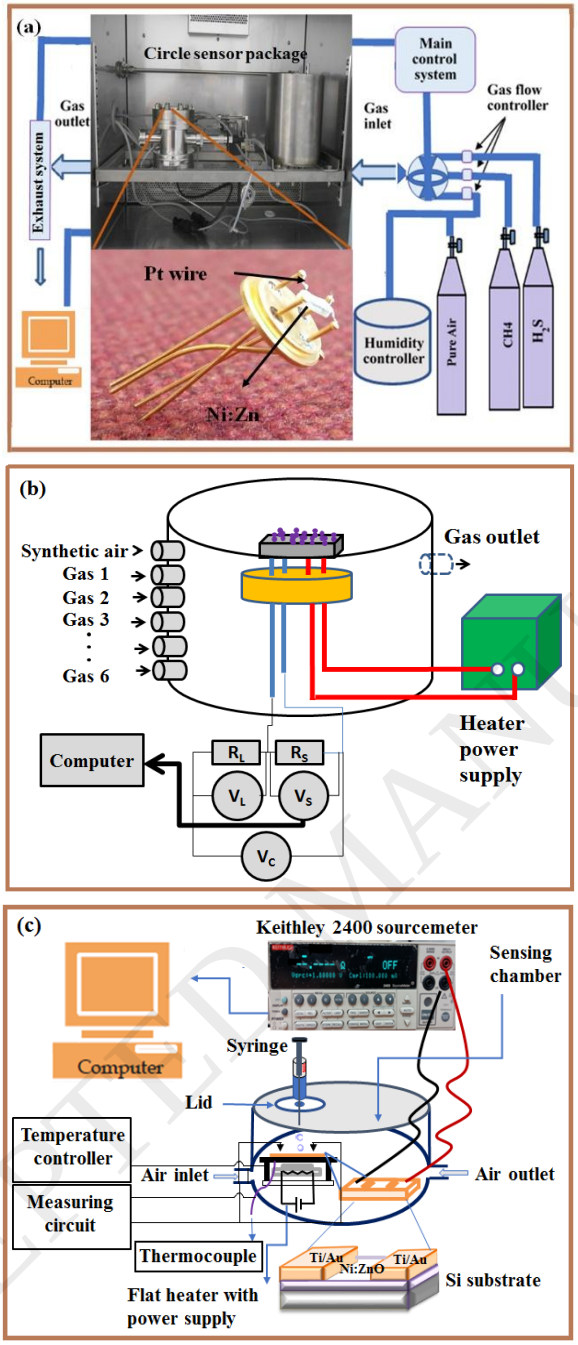

Fig. 1. Schematics of the experimental set-up for the gas sensing of the Ni-doped ZnO devices. (a) inorganic gas sensing along with a photograph of the side view of the sensor element package on a metal stent; (b) The measuring electronic circuit for the sensor testing equipment of Fig 1(a), (c) VOL gas sensing.

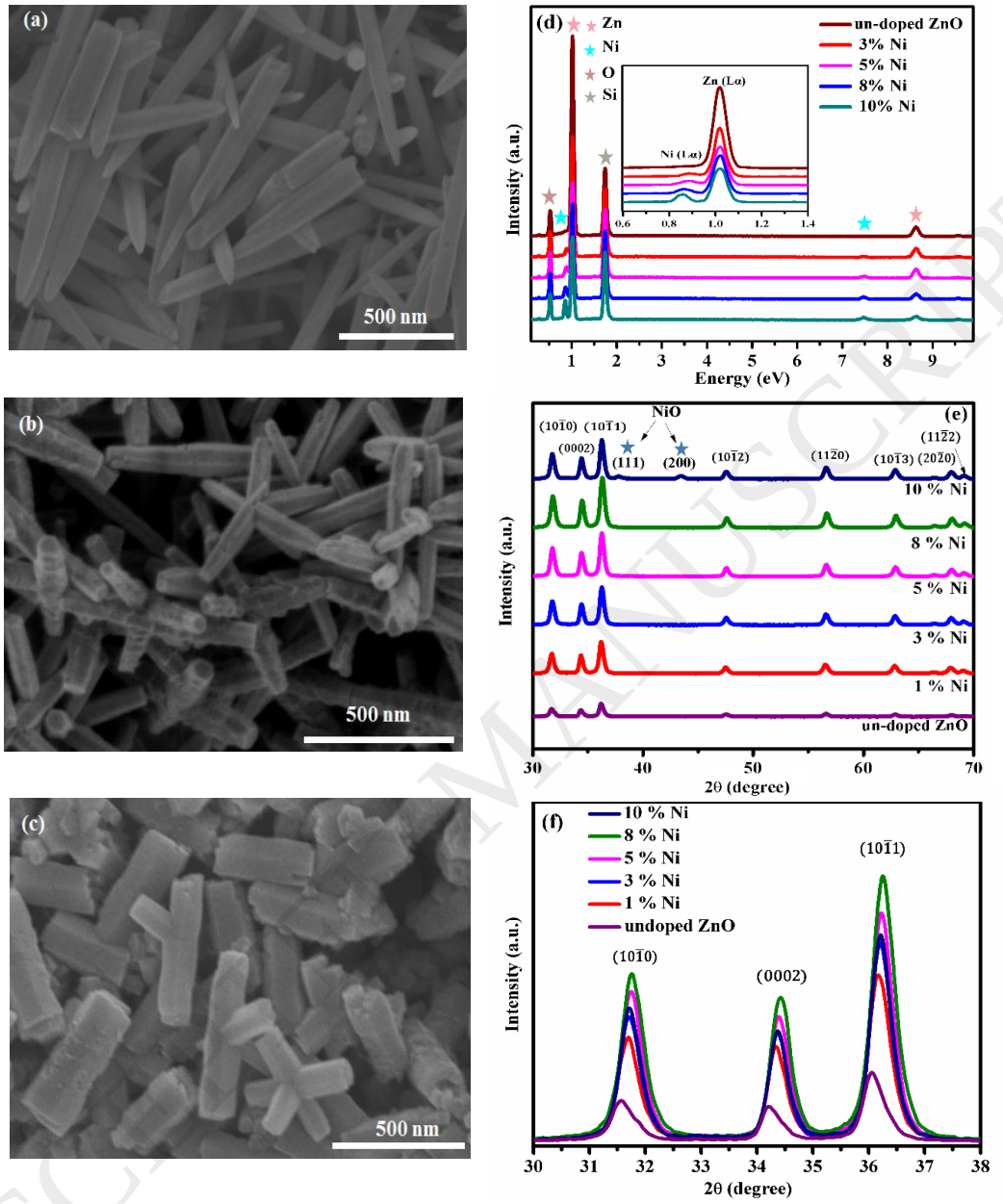

Fig. 2. SEM images of the as-grown (a) un-doped ZnO and (b) 8% (c) 10% Ni-doped ZnO NRs using home-made bimetallic metal-organic complexes as precursors. (d) x-ray energy dispersive spectra of the (0-10%) Ni doped ZnO NRs with inset showing enlarged spectra of Ni and Zn. (e) XRD patterns of the as-grown un-doped and Ni-doped ZnO NRs; (f) enlarged XRD patterns showing the shift in the first three peaks with Ni content.

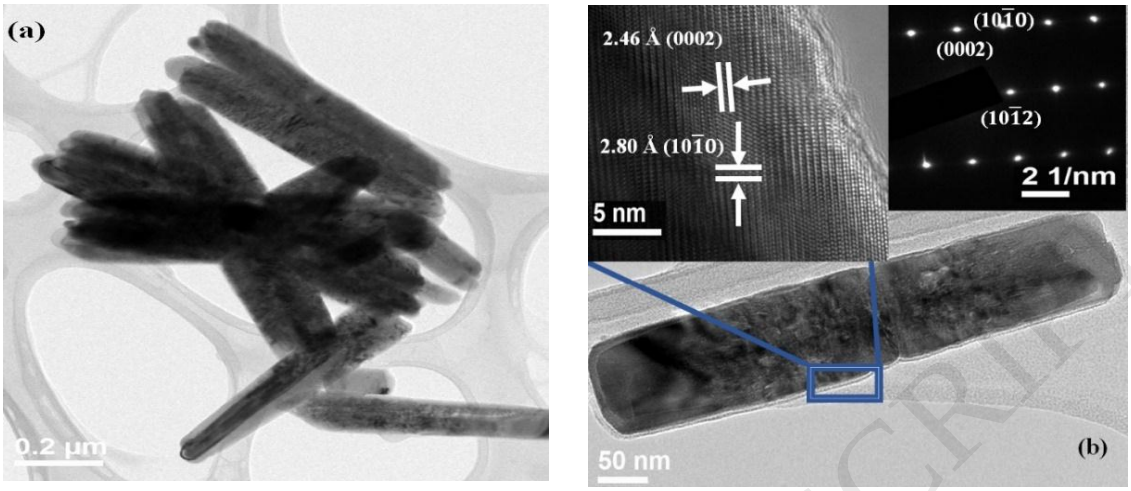

Fig. 3. (a) TEM image of a few NRs (5% Ni) (b) a high-magnification TEM image of a single NR, with right inset showing selected-area diffraction pattern and left inset showing a high-resolution TEM image taken from the marked region of Fig. 3b.

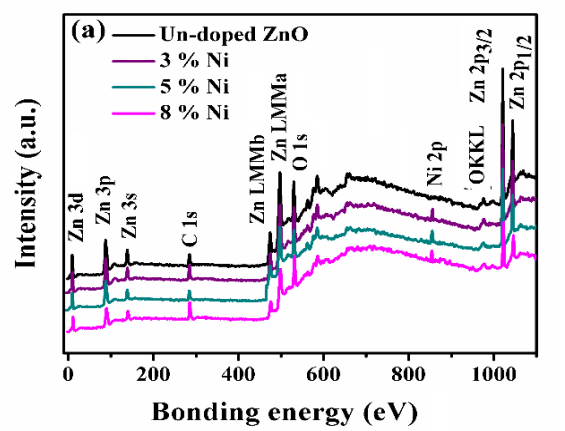

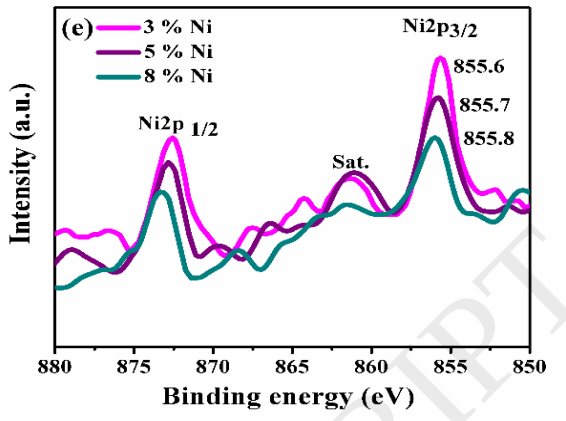

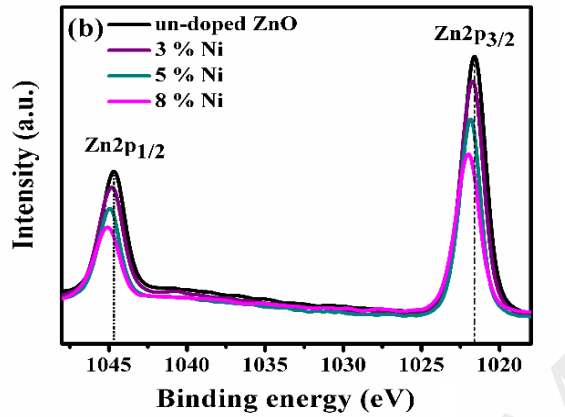

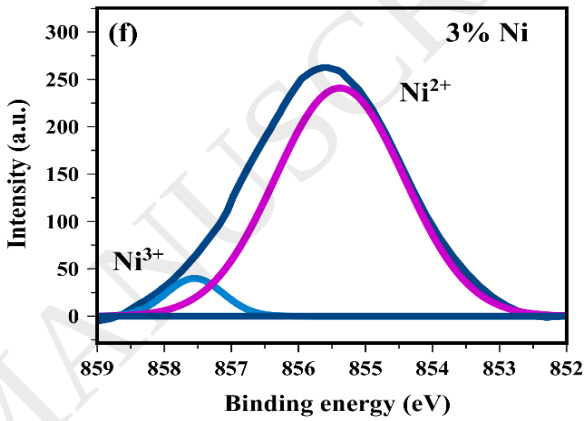

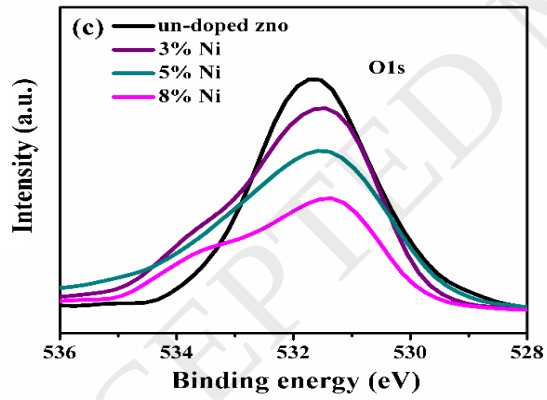

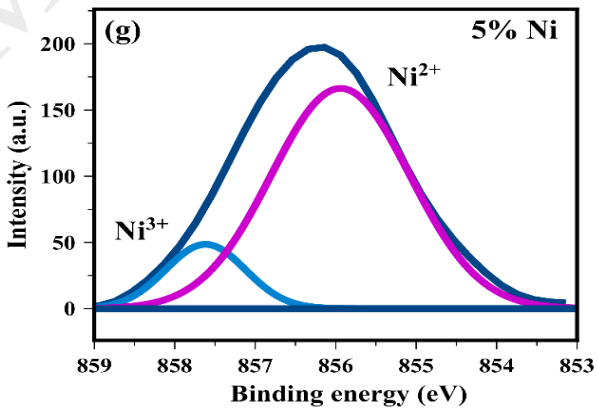

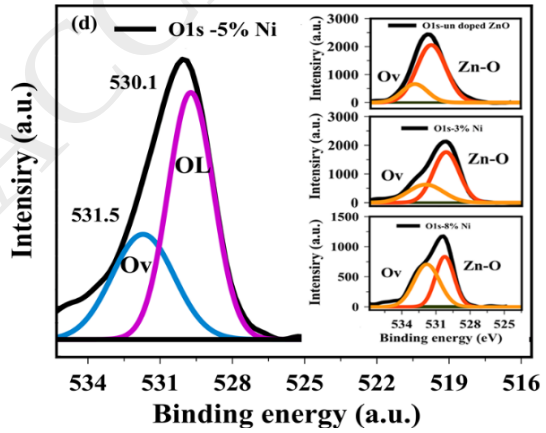

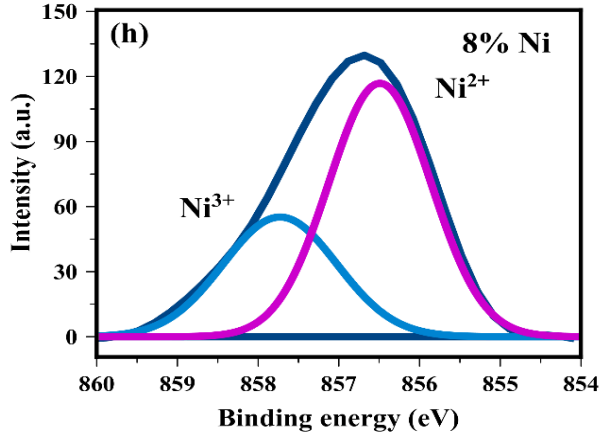

Fig. 4. Overlay graphs of the un-doped and Ni doped ZnO NRs for (a) full scan, (b) Zn $2p_{3/2}$ and $2p_{1/2}$ states and (c) O1s core level of the un-doped and Ni-doped ZnO NRs with 3%, 5%, and 8% Ni content (d) peak position and deconvolated O1s spectra of the 5% Ni content. The inset shows deconvoluted un-doped ZnO, 3% and 8% Ni content (e) $Ni2p_{3/2}$ and $2p_{1/2}$ states of the un-doped and Ni-doped ZnO NRs with 3%, 5%, and 8% Ni content, (f-h) enlarged and decomposed Ni $2p_{3/2}$ core level for Ni-doped ZnO NRs with Ni concentrations of 3%, 5 %, and 8 %, respectively.

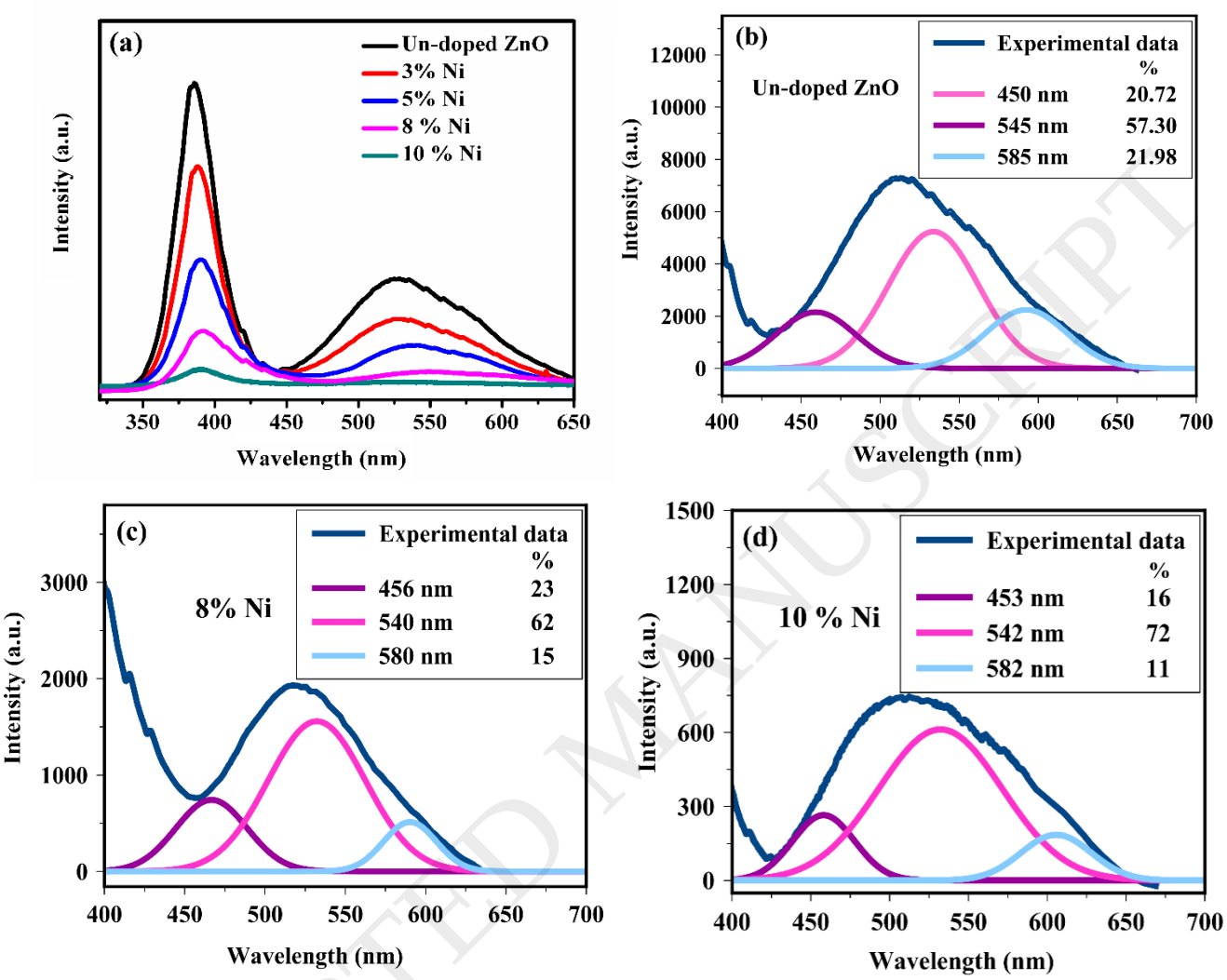

Fig. 5. Room temperature (23 °C) PL spectra of the (a) full spectrum of 0-10% Ni doped ZnO; (b,c,d) deconvolution of the visible emission for un-doped ZnO, 8%, and 10% Ni-doped ZnO NRs, respectively

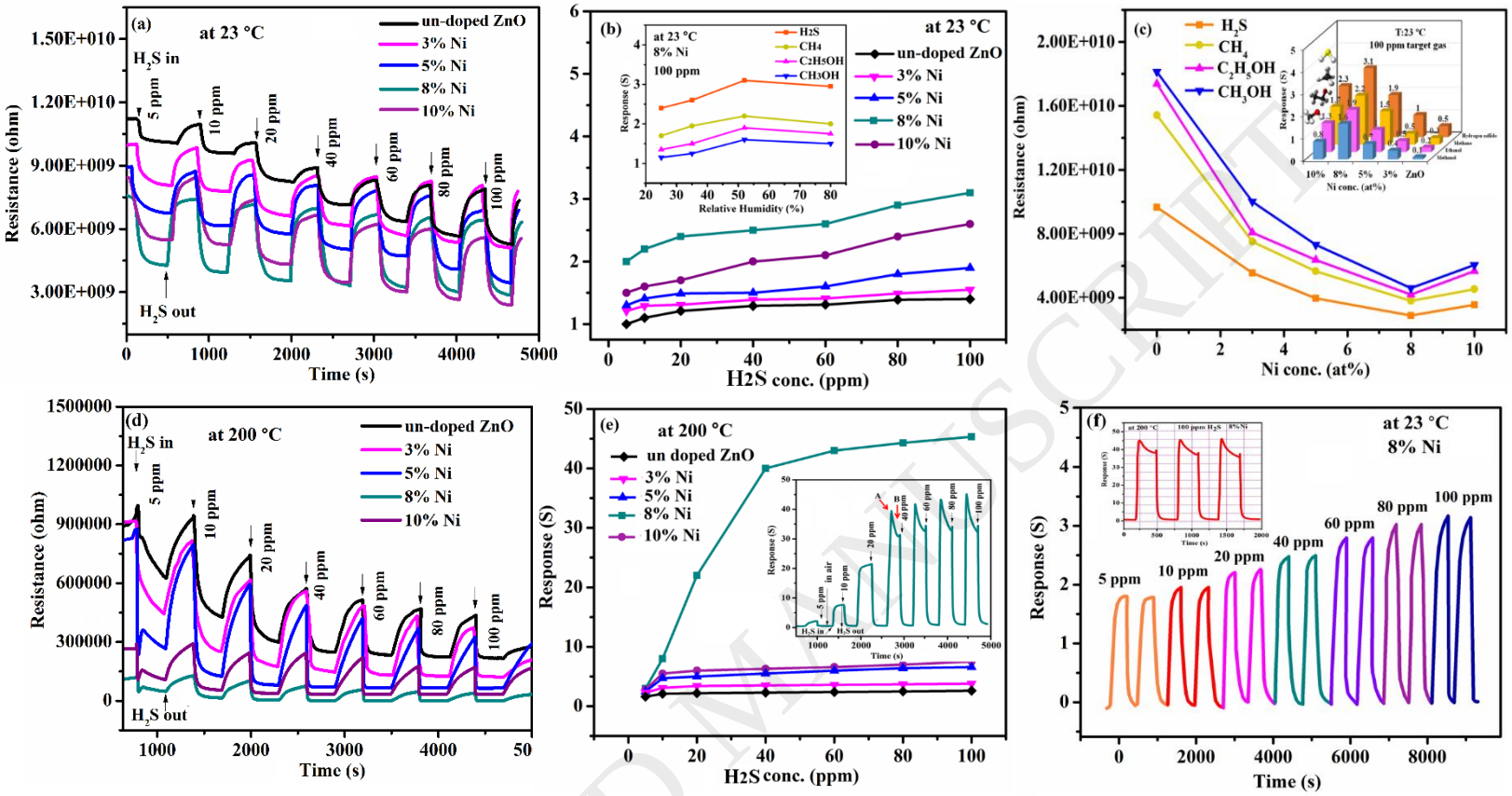

Fig. 6. (a) Transient resistance of undoped ZnO, 3%, 5%, 8% and 10% Ni-doped NR sensors upon exposure to (5-100 ppm) H_2S at 23 °C, (b) dynamic response of the (0-10%) Ni-doped ZnO NR sensor for H_2S at 23 °C, the inset shows sensor response to 100 ppm of H_2S, CH_4, CH_3OH and C_2H_5OH gases (8% Ni) for 25-80 % RH at 23 ºC. (c) resistance evolution of the Ni-doped NR sensor with various Ni concentrations in presence of 100 ppm at different gas species, the inset shows the histogram of its response, (d) transient resistance and (e) dynamic response of the (0-10%) Ni-doped ZnO NR sensor to (5-100 ppm) H_2S at 200 ºC, respectively. (f) repeatability test of the 8% Ni doped ZnO sensor to (5-100) ppm H_2S gas at 23 °C. the inset shows repeatability test to 100 ppm H_2S gas at 200 ºC.

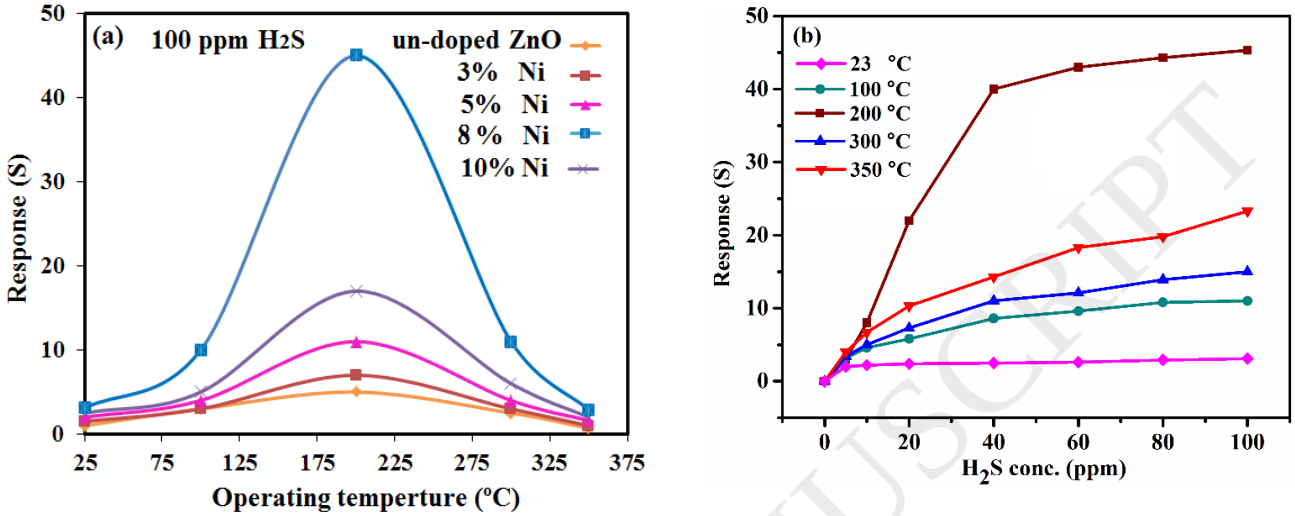

Fig. 7. (a) Response of various Ni doping ZnO NRs to 100 ppm H_2S gas as a function of operating temperature, (b) response as a function of H_2S concentration (5-100 ppm) at different operating temperatures for 8% Ni-doped ZnO NR sensor.

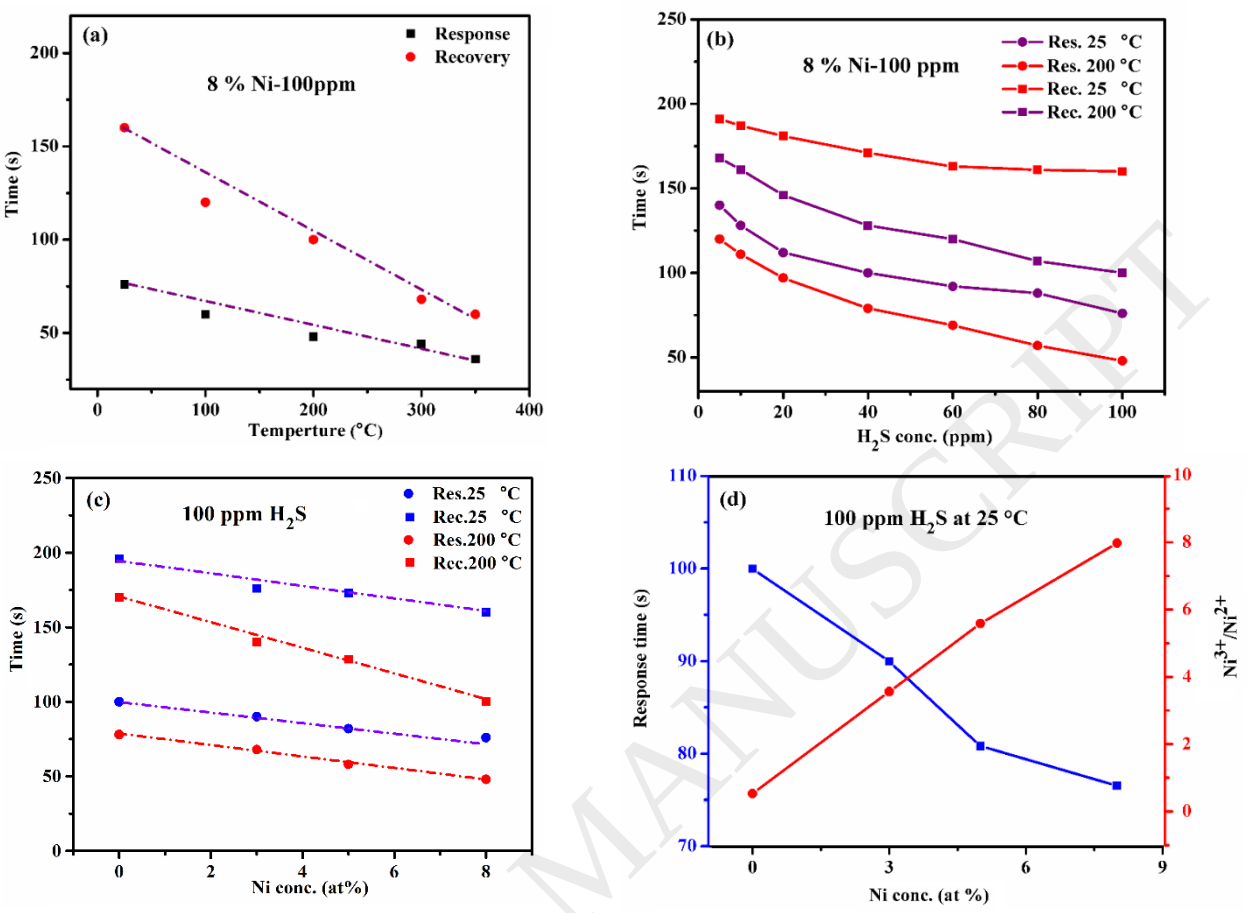

Fig. 8. (a) Response-recovery time as a function of operating temperature under 100 ppm H_2S for the 8% Ni-doped ZnO NRs sensor, (b) response-recovery time as a function of H_2S gas concentration for the 8% Ni doped ZnO NRs sensor at 23 °C and 200 °C, (c,d) response-recovery time as a function of Ni content in ZnO NRs under 100 ppm H_2S at 23 °C and 200 °C respectively, (e) estimating the relationship between response time and Ni^{3+}/Ni^{2+} ions ratio (in EDX) as a function of Ni content.

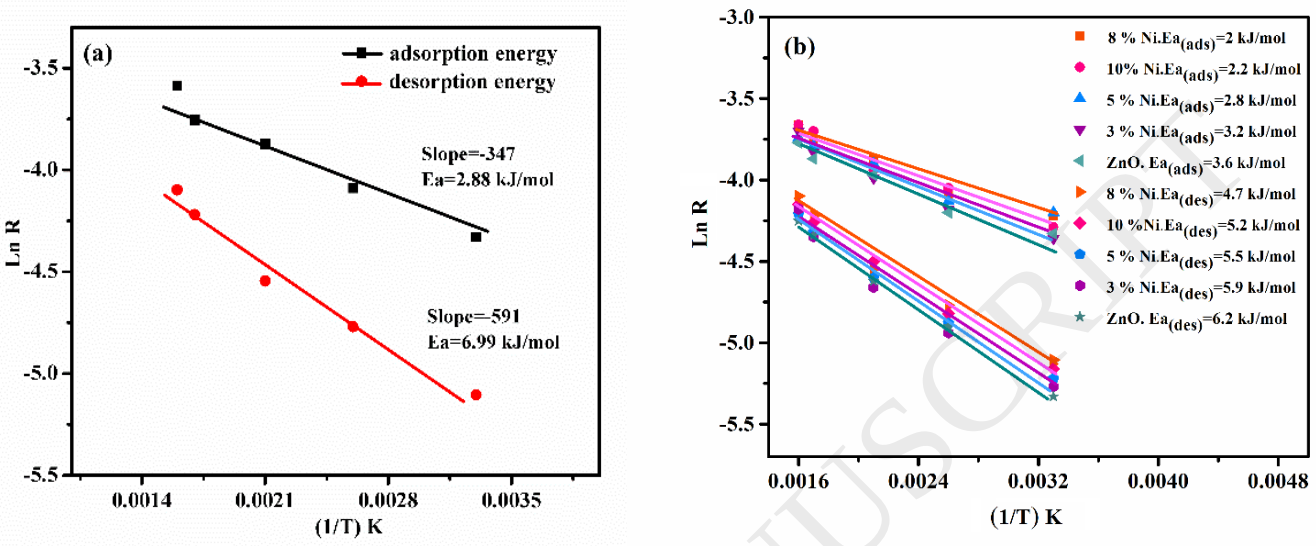

Fig. 9. (a) Arrhenius plot of Ln (R) vs 1/T for the 8% Ni-doped ZnO NR sensor after exposure to 100 ppm H_2S in a 23-350 $^{\circ}$C temperature range for deriving adsorption desorption energy, (b) the same Arrhenius plot of ln(R) vs 1/T for un-doped ZnO, 3%, 5%, 8%, and 10% Ni-doped ZnO NR sensors.

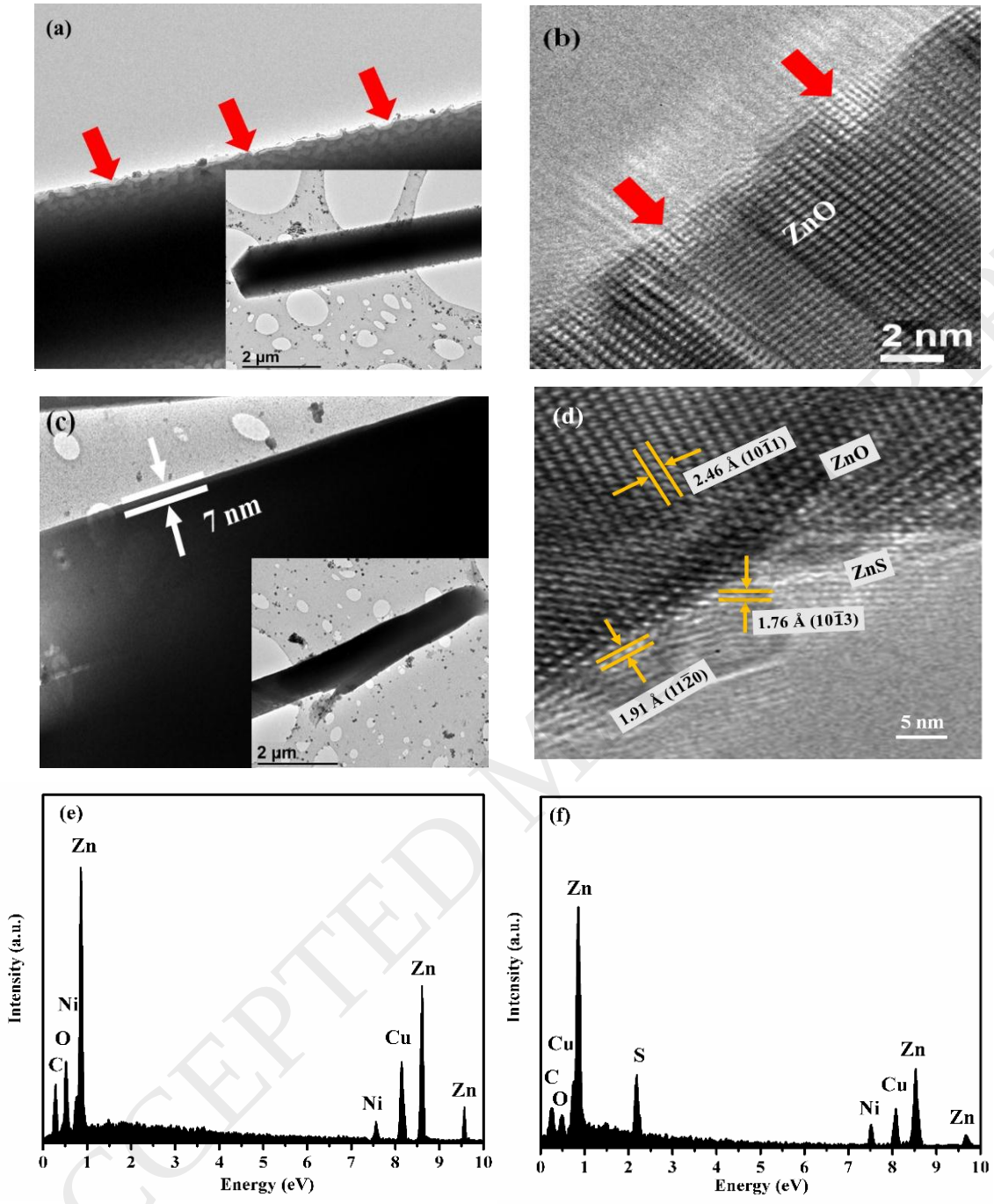

Fig. 10. (a) TEM image of the NR sensor before exposure to H_2S, (b) HR-TEM images corresponding to (a), (c) TEM image of the NR sensor after exposure to H_2S at 23 $^{\circ}$C for 3 hours, (d) corresponding HR-TEM images of (c). EDX analysis of (e) Fig. b, (f) Fig. d.

References

[1] K. Wetchaku, T. Samejai, N. Tamaekong, C. Lieuhiran, C. Siriwong, V. Kruefu, A. Wisitsoraat, A. Tuantranont, S. Phanichphant, Semiconducting metal oxides as sensors for environmentally hazardous gases, Sens. Actuators B. 160 **(**2011) 580-591.

[2] S. M. Kanan, O. M. El-Kadri, I. A. Abu-Yousef and M. C. Kanan, Semiconducting Metal Oxide Based Sensors for Selective Gas Pollutant Detection, Sensors. 9 (2009) 8158-8196.

[3] F.H. Ramirez, J. D. Prades and J. R. Morante, Sensor and materials. 21(2009) 219-227.

[4] Z. Guo, G. Chen, G. Zeng, L. Liu and Ch. Zhang, Metal oxides and metal salt nanostructures for hydrogen sulfide sensing: mechanism and sensing performance, RSC Adv. 5 (2015) 54793-54805.

[5] V. Galstyan, E. Comini, G. Faglia and G. Sberveglieri, Sensors. 13 (2013) 4813-14838.

[6] C. S. Rout, M. Hegde, C.N.R. Rao, H_2S sensors based on tungsten oxide nanostructures, Sens. Actuators B. 128 (2008) 488-493.

[7] L. Liao, H. B. Lu, J. C. Li, H. He, D. F. Wang, D. J. Fu, and C. Liu, Size Dependence of Gas Sensitivity of ZnO Nanorods, J. Phys. Chem. C. 111 (2007) 1900-1903.

[8] J. Liu, X. Huang, G. Ye, W. Liu, Z. Jiao, W. Ghao, Z. Zhou, and Z. Yu, H_2S Detection sensing Characteristic of CuO/SnO_2 Sensor, Sensors. 3 (2003) 110-118.

[9] Z. Sun, H. Yuan, Z. Liu, B. Han, and X. Zhang, A Highly Efficient Chemical Sensor Material for H_2S: a-Fe_2O_3 Nanotubes Fabricated Using Carbon Nanotube Templates, Adv. Mater. 17 (2005) 2993-2997.

[10] L. Mai, L. Xu, Q. Gao, C. Han, B. Hu, and Y. Pi, Single β-$AgVO_3$ Nanowire H_2S Sensor, Nano Lett. 10 (2010) 2604-2608.

[11] A. Wei, L. Pan, W. Huang, Recent progress in the ZnO nanostructure-based sensors, Materials Science and Engineering B. 176 (2011) 1409-1421.

[12] V. Galstyann, E. Comini, C. Baratto, G. Faglia, G. Sberveglieri, Nanostructured ZnO chemical gas sensors, Ceramics International. 41 (2015) 14239-14244.

[13] Z.S. Hosseini, A. Iraji zad, A. Mortezaali, Room temperature H_2S gas sensor based on rather aligned ZnO nanorods with flower-like structures, Sens. Actuators B. 207 (2015) 865-871.

[14] A. Kumar, N. Joshi, S. Samanta, A. Singh, A. K. Debnath, A. K.Chauhan, M. Roy, R. Prasad, K. Roy, M. M. Chehimi, D. K. Aswal, S. K. Gupta, Room temperature detection of H_2S by flexible gold-cobalt phthalocyanine heterojunction thin films, Sens Actuators B. 206 (2015) 653-662.

[15] Z. Song, Z. Wei, B. Wang, Z. Luo, S. Xu, W. Zhang, H. Yu, M. Li, Z. Huang, J. Zang, F. Yi, and H. Liu, Sensitive Room-Temperature H_2S Gas Sensors Employing SnO_2 Quantum Wire/Reduced Graphene Oxide Nanocomposites, Chem. Mater. 28 (2016) 1205-1212.

[16] A.A.M. Farag, M. Cavas, F. Yakuphanoglu, F.M. Amanullah, Photoluminescence and optical properties of nanostructure Ni doped ZnO thin films prepared by sol-gel spin coating technique, J. Alloys Compd. 509 (2011) 7900 -7908.

[17] K. Raja, P.S. Ramesh, D. Geetha, Synthesis, structural and optical properties of ZnO and Ni-doped ZnO hexagonal nanorods by Co-precipitation method, Spectrochimica Acta Part A: Molecular and Biomolecular Spectroscopy. 120 (2014) 19-24.

[18] P. Hu, N. Han, D. Zhang, J. C. Ho, Y. Chen, Highly formaldehyde-sensitive, transition-metal doped ZnO nanorods prepared by plasma-enhanced chemical vapor deposition, Sens. Actuators B: Chemical. 169 (2012) 74-80.

[19] K.G. Girija, K. Somasundaram, Anita Topkar, R.K. Vatsa, Highly selective H_2S gas sensor based on Cu-doped ZnO nanocrystalline films deposited by RF magnetron sputtering of powder target, J. Alloys Compd. 684 (2016) 15-20.

[20] R. Saravanan, K. Santhi, N. Sivakumar, V. Narayanan, A. Stephen, Synthesis and characterization of ZnO and Ni doped ZnO nanorods by thermal decomposition method for spintronics application, Material characterization. 67 (2012) 10-16.

[21] J. Rebholz, K. Grossmann, D. Pham, S. Pokhrel, L. Mädler, U. Weimar and N. Barsan, Selectivity Enhancement by Using Double-Layer MOX-Based Gas Sensors Prepared by Flame Spray Pyrolysis (FSP), Sensors. 16 (2016) 1437(1-9).

[22] M. R. Modaberi, S. Brahma, R. Rooydell, R. C. Wang, C. P. Liu, Novel hybrid transition metal complexes of diaquabis (acetylacetonato-κ^2o,o′)[nickel(II)/zinc (II)] as solid metal-organic

precursors: Synthesis, properties and magnetic response, Appl Organometal Chem. 3746 (2017) 1-12.

[23] J. J. Wu and S. C. Liu, Heterostructures of ZnO-Zn coaxial nanocables and ZnO nanotubes, Appl. Phys. Lett. 81 (2002) 1312.

[24] S. Kumar, P. Vats, S. Gautam, V.P. Gupta, K.D. Verma, K.H. Chae, M. Hashim, H.K. Choi, Electronic structure, magnetic and structural properties of Ni doped ZnO nanoparticles, Materials Research Bulletin. 59 (2014) 377-381.

[25] B. Singh, A. Kaushal, I. Bdikin, K. V. Saravanan, J.M.F. Ferreira, Effect of Ni doping on structural and optical properties of Zn1-xNixO nanopowder synthesized via low cost sono-chemical method, Materials Research Bulletin. 70 (2015) 430-435.

[26] B. Pal, D. Sarkar, P.K. Giri, Structural, optical, and magnetic properties of Ni doped ZnOnanoparticles: Correlation of magnetic moment with defect density, Applied Surface Science. 356 (2015) 804-811.

[27] M. S. Abdel-wahab, A. Jilani, I.S. Yahia, A. A. Al-Ghamdi., Enhanced the photocatalytic activity of Ni-doped ZnO thin films: Morphological, optical and XPS analysis, Superlattices and Microstructures. 94 (2016) 108-118.

[28] W. Shan, W. Walukiewicz, J. W. Ager, K. M. Yu, H. B. Yuan, H. P. Xin, G. Cantwell, and J. J. Song, Nature of room-temperature photoluminescence in ZnO, Appl. Phys. Lett. 86 (2005) 191911 (1-3).

[29] C. V. Manzano, D. Alegre, O. Caballero-Calero, B. Alén, and M. S. Martín-González, Synthesis and luminescence properties of electrodeposited ZnO films, J. Appl. Phys. 110 (2011) 043538 (1-8).

[30] J. Iqbal, B. Wang, X. Liu, D. Yu, B. He and R. Yu, Oxygen-vacancy-induced green emission and room-temperature ferromagnetism in Ni-doped ZnO nanorods, New Journal of Physics. 11 **(**2009) 1-12.

[31] S. Brahma, J. Khatei, S. Sunkara, K. Y. Lo and S. A. Shivashankar, Self-assembled ZnO nanoparticles on ZnO microsheet: ultrafast synthesis and tunable photoluminescence properties, J. Phys. D: Appl. Phys. 48 (2015) 225305 (12pp).

[32] L. S. Vlasenko and G. D. Watkins, Optical detection of electron paramagnetic resonance in room-temperature electron-irradiated ZnO, Physical Review B. 71 (2005) 125210 (1-6).

[33] Y. Wang, G. Duan, Y. Zhu, H. Zhang, Z. Xu, Z. Dai, W. Cai, Room temperature H_2S gas sensing properties of In_2O_3 micro/nanostructured porous thin film and hydrolyzation-induced enhanced sensing mechanism, Sens. Actuators B. 228 (2016) 74-84.

[34] N.H. Al-Hardan, M.J. Abdullah, A. Abdul Aziz, Performance of Cr-doped ZnO for acetone sensing, Applied Surface Science. 270 (2013) 480- 485.

[35] Z. Li, Y. Huang, S. Zhang, W. Chen, Z. Kuang, D. Ao, W. Liu, Y. Fu, A fast response & recovery H_2S gas sensor based on α-Fe_2O_3 nanoparticles with ppb level detection limit, Journal of Hazardous Materials. 300 (2015) 167-174.

[36] L. Geng, X. Huang, Y. Zhao, P. Li, S. Wang, S. Zhang, S. Wu, H_2S sensitivity study of polypyrrole/WO_3 materials, Solid-State Electronics. 50 (2006) 723-726.

[37] G. Cui, M. Zhang and G. Zou, Resonant tunneling modulation in quasi-2D Cu_2O/SnO_2 p-n horizontal multi- layer heterostructure for room temperature H_2S sensor application, Science Report. 3 (2013) 1250 (1-8).

[38] V. D. Kapse, S.A. Ghosh, G.N. Chaudhari, F.C. Raghuwanshi, D.D. Gulwade, H_2S sensing properties of La-doped nanocrystalline In_2O_3, Vacuum. 83 (2009) 346-352.

[39] L. Geng, Gas sensitivity study of polypyrrole/WO_3 hybrid materialstoH_2S, Synthetic Metals. 160 (2010) 1708-1711.

[40] Z. Li, Y. Huang, S. Zhang, W. Chen, Z. Kuang, D. Ao,W. Liu, Y. Fu, Journal of Hazardous Materials 300 (2015) 167-174.

[41] L. Wang, Y. Kang, Y. Wang, B. Zhu, S. Zhang, W. Huang, S. Wang, CuO nanoparticle decorated ZnO nanorod sensor for low-temperature H_2S detection, Materials Science and Engineering C. 32 (2012) 2079-2085.

[42] J. Kim and K. Yong, Mechanism Study of ZnO Nanorod-Bundle Sensors for H_2S Gas Sensing, J. Phys. Chem. C. 115 (2011) 7218-7224.

[43] M. Zhao, X. Wang, L. Ning, J. Jia, X. Li, L. Cao, Electrospun Cu-doped ZnO nanofibers for H_2S sensing, Sens. Actuators B. 156 (2011) 588-592.

[44] N. M. Vuong, N. D. Chinh, B. T. Huy and Y. I. Lee, CuO-Decorated ZnO Hierarchical Nanostructures as Efficient and Established Sensing Materials for H_2S Gas Sensors, Scientific Reports. 6 (2016) 26736 (1-13).

[45] G. Qi, L. Zhang, and Z. Yuan, Improved H_2S gas sensing properties of ZnO nanorods decorated by a several nm ZnS thin layer, Phys. Chem. Chem. Phys. 16 (2014) 13434-13439.

[46] B. P. Dhonge, S. S. Ray and B. Mwakikunga, Electronic to protonic conduction switching in Cu_2O nanostructured porous films: the effect of humidity exposure, RSC Adv. 7 (2017) 21703-21712.

[47] P. K. Kannana, R. Saraswathia, J. B. B. Rayappan, A highly sensitive humidity sensor based on DC reactive magnetron sputtered zinc oxide thin film, Sens. Actuators A. 164 (2010) 8-14.

[48] B.C. Yadav, R. Srivastava, C.D. Dwivedi, Synthesis and characterization of ZnO-TiO_2 nanocomposite and its application as a humidity sensor, Philos. Mag. 88 (2008) 1113-1124.

Biographies

Matin Roshanzamir Modaberi received her M.S degree in Organic chemistry in 2008, focusing on the magnetic field of heteroaromatic ring systems. In 2013 She joined to materials science and engineering department. Currently she is a doctoral researcher under the supervision of Prof. Chuan-Pu-Liu in National Cheng Kung University, Taiwan. Her current research interest includes experimental surface physics, thin films, nanotechnology, synthesis and characterization of different kind of semiconductor oxide heterostructures (bimetallic) for optoelectronics, magnetic and sensing applications.

Reza Rooydell was born in Yasoj, Iran in 1976.He completed his Ph.D. from National Cheng Kung University University, Taiwan in 2017. The major field in his Ph.D. was synthesis and growth of heterostructure precursors for their applications in photocatalytic, luminescence and gas sensing properties.

Sanjaya Brahma has received Ph.D from Indian Institute of Science (IISC), India in 2011, followed by a master's degree (M. Tech) in 2004 from Indian Institute of Technology, Kharagpur, India. Currently, he is working as a post-doctoral fellow in National Cheng Kung University, Taiwan. He researches interest is mainly growth/ characterization of semiconductor oxide nanostructures and graphene-metal oxide composite for applications in optoelectronics, gas sensor, and Li ion batteries.

Amos A. Akande has completed his Ph.D from CSIR national center for nanostructured materials, South Africa. He is working as a post-doctoral fellow at the same place. His current research involves growth and characterization of V_2O_5 thin films/nanostructures and multi-walled carbon nanotubes for gas sensor.

Bonex Mwakikunga completed his PhD in Physics at the University of the Witwa-tersrand, Johannesburg in 2009, went to pursue a post-doctoral fellowship at the CSIR – National Laser Centre in 2010. He is employed at the CSIR – National Center for Nano-Structured Materials since then where he is leading a Nano Sensors Programme. He is a co-editor of OA Tube Nanotechnology and a guest editor of the Sensor and Transducers journal. His current interest is in developing materials for gas sensors with application to sensors in the medical field

Chuan-Pu Liu received his PhD in Materials Science and Metallurgy in 1999 from the University of Cambridge in UK. He did post-doctoral research in University of Illinois at Urbana-Champaign for two years before joining the faculty in the Department of Materials Science and Engineering at National Cheng Kung University in Taiwan in 2000. His lab is currently interested in growth, characterization and applications of semiconductor nanomaterials, with focus on gas sensors, negative electrodes in lithium-ion batteries, piezotronic devices and thermoelectric devices. He is currently a distinguished professor leading a lab working on semiconductor nanomaterials in the Department of Materials Science and Engineering at National Cheng Kung University in Taiwan.